Nano Research Energy

ISSN 2791-0091 (print); 2790-8119 (online)
https://doi.org/10.26599/NRE.2022.9120027

Research Article

Metal-coordinated porous polydopamine nanospheres derived Fe_3N-FeCo encapsulated N-doped carbon as a highly efficient electrocatalyst for oxygen reduction reaction

Fanjuan Guo[1], Mingyue Zhang[2], Shicheng Yi[1], Xuxin Li[1], Rong Xin[1], Mei Yang[1], Bei Liu[1], Hongbiao Chen[1] (✉), Huaming Li[1], and Yijiang Liu[1] (✉)

[1] *College of Chemistry and Key Laboratory of Environmentally Friendly Chemistry and Application of Ministry of Education, Xiangtan University, Xiangtan 411105, China*
[2] *School of Materials Science and Engineering, Georgia Institute of Technology, Atlanta, GA 30332, USA*

Received: 23 July 2022 / Revised: 11 August 2022 / Accepted: 15 August 2022

ABSTRACT

The exploration of high-efficiency, long-durability, and cost-effectiveness transition metal doped carbon materials to replace the commercial Pt/C in oxygen reduction reaction (ORR) is greatly desirable for promoting the advancement of sustainable energy devices. Herein, the Fe_3N and FeCo alloy decorated N-doped carbon hybrid material (denoted Fe_3N-FeCo@NC) is prepared and applied as the ORR catalyst, which is derived from the two-step pyrolysis of an intriguing complex consisted of metal-coordinated porous polydopamine (PDA) nanospheres (i.e., Fe-PDA@Co) and melamine. The resulting Fe_3N-FeCo@NC delivers outstanding ORR activity with an onset potential (E_{on}) of 1.05 V, a half-wave potential ($E_{1/2}$) of 0.89 V, as well as excellent long-term stability and methanol resistance over Pt/C. Interestingly, the home-made Zn-air battery with Fe_3N-FeCo@NC as the air-cathode demonstrates much higher open-circuit voltage (1.50 vs. 1.48 V), power density (141 vs. 113 $mW{\cdot}cm^{-2}$) and specific capacity (806.6 vs. 660.6 $mAh{\cdot}g^{-1}_{Zn}$) than those of Pt/C counterpart. Such a remarkable ORR activity of Fe_3N-FeCo@NC may stem from the synergistic effect of Fe_3N and FeCo active species, the large surface area, the hierarchical porous structure and the exceptional sphere/sheet hybridized architecture.

KEYWORDS

porous polydopamine nanospheres, melamine, *in-situ* synthesis, Fe_3N-FeCo nanoparticles, oxygen reduction reaction (ORR) electrocatalyst

1 Introduction

As the growing deterioration of environmental issues stems from the intensified utilization/exploration of fossil fuels, the development of clean and sustainable energy conversion and storage techniques has garnered worldwide scientific and industrial attention. The oxygen reduction reaction (ORR) is a critical half-reaction involved in renewable energy conversion and storage devices, such as fuel cells and Zn-air batteries [1–3]. Nonetheless, the sluggish ORR kinetics at the cathode leads to insufficient overall energy conversion efficiency, and thus numerous endeavors have been made to boost ORR kinetics. Up to now, Pt-based precious metals are confirmed to be the state-of-the-art electrocatalysts to accelerate ORR efficiently, but the high cost, low reserves, deficient durability as well as poor methanol tolerance have largely obstructed the commercial-scale application [4–6]. Accordingly, a rich variety of non-precious electrocatalysts with competitive activity and excellent stability have been extensively explored in the past several years.

Among various non-precious electrocatalysts, transition metal nitrides incorporated carbon materials (MN_x-C) have become prospective alternatives to replace Pt-based precious electrocatalysts owing to their high conductivity, economical cost and intriguing ORR performance [7, 8]. Particularly, FeN_3-decorated carbon materials (Fe_3N-C) demonstrated comparable ORR activity to Pt/C [9, 10], and FeN_3 nanoparticles (NPs) have been substantiated to be genuine active species toward ORR [11]. However, the inevitable aggregation of FeN_3 during the reaction can obviously decrease its activity and stability. To further optimize the ORR performance of Fe_3N-C, investigators have developed an *in-situ* nitridation method with NH_3 at high temperature to form small Fe_3N NPs [12, 13]. For another, the morphology and porosity engineering of carbon matrix is also beneficial to the ORR performance of Fe_3N-C. For example, by using chitosan and $K_3[Fe(CN)_6]$ as raw materials, the Fe_3N@N-C catalyst was prepared by a hydrogel-bridged nitridation method, which displayed a positive half-wave potential toward ORR over Pt/C [14]. By

Address correspondence to Hongbiao Chen, chenghongbiao@xtu.edu.cn; Yijiang Liu, liuyijiang84@xtu.edu.cn

using a three-dimensional (3D) zeolitic-imidazole framework (ZIF) as a scaffold, Amr Radwan and coworkers fabricated Fe_3N NPs encapsulated carbon frameworks (ZFN-900), which displayed a higher ORR activity than carbon-supported Pt [15]. In such cases, however, the additional nitridation process performed in NH_3 atmosphere at high temperature is usually dangerous and can increase the manufacturing costs. Recently, Wang's group has indicated that the combination of Fe_3N and alloy NPs facilitates the ORR catalytic activity of the resultant catalyst due to the improved electroconductivity and the promoted charge transfer at the heterogeneous interface. Surprisingly, researches on the fabrication of such Fe_3N-C with heterogeneous interface are comparatively few and limited in scope [16]. By comprehensively evaluating of catalytic activity and costs, the development of *in-situ* preparation of Fe_3N (i.e., without additional nitridation) and alloy NPs embedded carbon materials with outstanding activity and stability for ORR is still highly desirable.

Herein, we report a facile and reliable strategy for the preparation of Fe_3N and FeCo alloy decorated N-doped carbon hybrid material (denoted Fe_3N-FeCo@NC) as a highly efficient ORR electrocatalyst for Zn-air batteries. Specifically, Fe-coordinated porous polydopamine (Fe-PDA) nanospheres were first synthesized by emulsion assembly strategy using Pluronic F127 and 1,3,5-trimethylbenzen (TMB) as surfactants and pore-forming agents. Co ions and melamine were sequentially added, forming the complex of Fe-PDA@Co@melamine through coordination interaction. The Fe_3N-FeCo@NC catalyst was produced after two-step carbonation of the Fe-PDA@Co@melamine complex. The utilization of porous Fe-PDA represents the critical point to our strategy owing to that the Fe-PDA acts as Fe, C and N sources, imparting the possibility to create Fe_3N without additional nitridation. Meanwhile, the porous structure helps to enlarge the surface area and promotes the exposure of the active species. It is noteworthy that the incorporation of melamine is of great significance to gaining sphere- and sheet-hybridized carbon materials with increasing N-content. The resultant Fe_3N-FeCo@NC catalyst shows a remarkable activity toward ORR with a +40 mV higher half-wave potential ($E_{1/2}$ = 0.89 V) than Pt/C ($E_{1/2}$ = 0.85 V) in alkaline medium. The long-term stability and methanol tolerance of Fe_3N-FeCo@NC are significantly improved compared to Pt/C.

2 Experimental

2.1 Synthesis of Fe-PDA

Fe-coordinated polydopamine porous nanospheres (Fe-PDA) were prepared by emulsion assembly [17, 18] and copolymerization strategy. First, dopamine (DA) (400 mg) and Pluronic F127 (800 mg) were dissolved in 100 mL water and ethanol (volume ratio of 1: 1), and then TMB (1.6 mL) was slowly dropped to form an emulsion under vigorous stirring. After 30 min, 10 mg $Fe(NO_3)_3{\cdot}9H_2O$ was quickly added, forming a complex of Fe-dopamine (Fe-DA) immediately. The tris solution was sequentially introduced to accelerate polymerization of the Fe-dopamine complex. A brown-black precipitate (denoted Fe-PDA) was collected after 2 h by centrifugation, and washed with water and ethanol. The sample was dried in a vacuum at 40 °C.

2.2 Synthesis of Fe-PDA@Co@melamine

Typically, 50 mg Fe-PDA powder was uniformly dispersed in 30 mL n-hexane, and a methanol solution containing 7.8 mg $Co(NO_3)_2$ (25 mg·mL^{-1}) was gradually added under ultrasonication at room temperature. After stirring for 2 h, Co ions were fully coordinated with Fe-PDA porous nanospheres, thus yielding the Fe-PDA@Co complex. Next, the melamine solution (500 mg, dissolved into 20 mL methanol and water) was added to the Fe-PDA@Co mixture, and the mixture was heated to 60 °C. After stirring overnight, the solvents were evaporated and a brown powder of Fe-PDA@Co@melamine was yielded. To investigate the influence of metal content on ORR performance of the as-prepared samples, different amounts of Fe and Co-loaded Fe-PDA-*x*@Co-y@melamine precursors were prepared by tuning the mass of $Fe(NO_3)_3$ and $Co(NO_3)_2$, where *x* denotes the molar ratio of $Fe(NO_3)_3$ to DA in the precursor Fe-PDA (*x* = 0.007, 0.01, and 0.012), and y denotes the content of $Co(NO_3)_2$ added to 50 mg Fe-PDA (*y* = 0.10, 0.15, 0.20, and 0.30).

2.3 Fabrication of Fe_3N-FeCo@NC

Specifically, a porcelain boat containing Fe-PDA-0.01@Co-0.15@melamine was pyrolyzed in a tubular furnace in two consecutive steps (550 °C/2 h, 800 °C/5 h) at 5 °C·min^{-1} under nitrogen flow. The Fe, Co and N co-doped porous carbon material was labelled as Fe_3N-FeCo@NC. For comparison, Fe-PDA-*x*@Co-*y*@melamine, Fe-PDA and Fe-PDA@Co were also carbonized under identical condition. The obtained catalysts were named Fe_3N-FeCo@NC-*x*-*y*, Fe/NC and FeCo/NC.

3 Results and discussion

3.1 Synthesis and characterization of Fe-PDA@Co@melamine

The synthetic route to Fe_3N-FeCo@NC is shown in Scheme 1. At first, DA and Pluronic F127 are dissolved in the H_2O-ethanol mixed solvents, and TMB is added under vigorous stirring to form stable emulsion micelles, where TMB and the intermediate blocks of F127 serve as the inner oil phase and the hydrophilic F127 blocks and DA face to the water phase. The color of the mixture turns into light green after the introduction of $Fe(NO_3)_3{\cdot}9H_2O$, suggesting the formation of Fe-DA complex. The polymerization of Fe-DA is obviously accelerated by the sequential addition of a tris solution, and

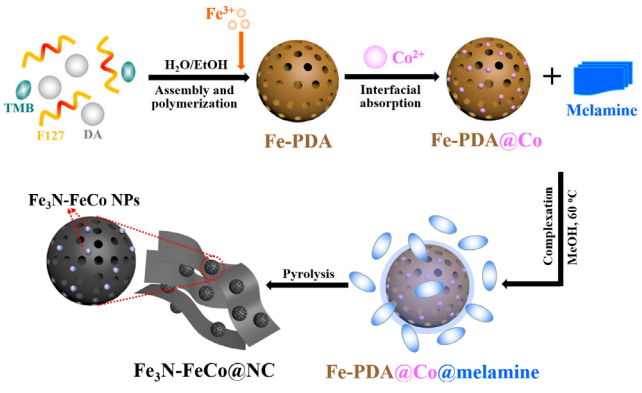

Scheme 1 The schematic illustration of the synthetic route to Fe_3N-FeCo@NC.

the brown-black precipitate denoted Fe-PDA is collected after 2 h. Fe-PDA@Co nanospheres are obtained through the interfacial interaction between Co^{2+} in methanol with Fe-PDA in n-hexane, where Co^{2+} is mainly absorbed on the surface of Fe-PDA nanospheres. After the addition of melamine methanol solution to the Fe-PDA@Co mixture and then heated to 60 °C for 24 h, the Fe-PDA@Co@melamine composites are thus created.

Subsequently, the Fe_3N and FeCo NPs encapsulated carbon material is derived by the two-step pyrolysis (i.e., 550, and 800 °C/2 h), where carbon nanosheets originated from melamine are hybridized with porous carbon nanospheres stemmed from Fe-PDA@Co.

The morphology of the porous Fe-PDA is depicted in Figs. 1(a) and 1(b). The average diameter of Fe-PDA nanospheres is approximately 100 nm, and the pores are clearly distinguished by the red circles. The incorporation of Co on Fe-PDA exhibits negligible morphology change (Fig. S1 in the Electronic Supplementary Material (ESM)). After the addition of melamine, the Fe-PDA@Co nanospheres are coexisted with melamine as shown in Fig. 1(c). The possible reason is that a small amount of melamine can coordinate with metal ions on porous PDA, and the remaining large amount of melamine may warp the metal-coordinated PDA nanospheres, thus forming irregular and aggregated particles. The composition of the Fe-PDA, Fe-PDA@Co and Fe-PDA@Co@melamine composites are characterized by Fourier-transform infrared spectroscopy (FTIR). As shown in Fig. S2 in the ESM, compared with the pristine PDA, the Fe-PDA displays slightly changed bands at 1,547, 1,483, 1,395 and 1,287 cm^{-1}, which are attributed to the indolyl and hydroxyl groups in PDA, indicating the coordination of Fe and PDA [19]. For Fe-PDA@Co, the characteristic bands of indolyl and hydroxyl groups in Fe-PDA are shifted to 1,551, 1,493, 1,400 and 1,290 cm^{-1}, indicating Co ions are coordinated with Fe-PDA [20]. All the feature bands of Fe-PDA@Co and melamine are involved in the FTIR spectrum of Fe-PDA@Co@melamine as indicated by the gray and pink boxes shown in Fig. 1(d). Notably, the symmetrical/asymmetrical stretching vibration (υ) and deformation vibration (δ) of C–H bonds in PDA combined with the emerging Co–N band successfully substantiate the formation of Fe-PDA@Co@melamine composites [21]. By varying the Fe and Co content, various Fe-PDA-*x*@Co-y@melamine composites can be facilely prepared, where x represents the molar ratio of $Fe(NO_3)_3$ to DA in Fe-PDA, and y denotes the content of $Co(NO_3)_2$ added to 50 mg Fe-PDA. When x = 0.01 and y = 0.15, the composites are abbreviated as Fe-PDA@Co@melamine, and the resulting carbon material is denoted as Fe_3N-FeCo@NC because this kind of catalyst possesses the optimal ORR performance (will be discussed later).

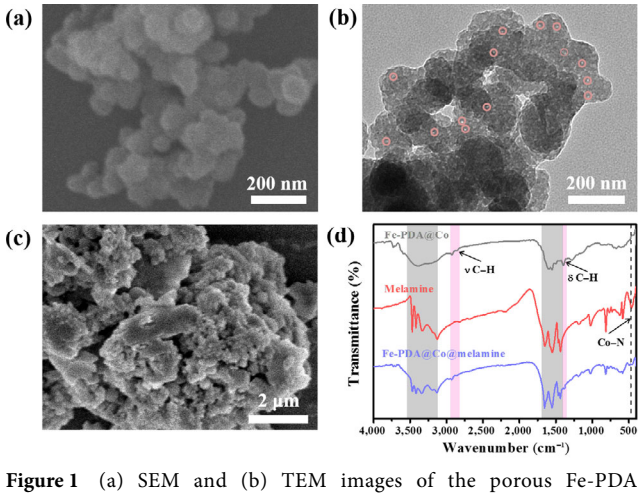

Figure 1 (a) SEM and (b) TEM images of the porous Fe-PDA nanospheres. (c) SEM image of Fe-PDA@Co@melamine composites, and (d) FTIR spectra of Fe-PDA@Co, melamine and Fe-PDA@Co@melamine composites.

3.2 Synthesis and characterization of Fe_3N-FeCo@NC

Through step-wise pyrolysis of Fe-PDA@Co@melamine composites, i.e., 550 °C for 2 h at the first stage and 800 °C for 2 h at the second stage, the Fe_3N-FeCo@NC electrocatalyst is thus derived. The crystal structure of Fe_3N-FeCo@NC was first examined by X-ray diffraction (XRD). As shown in Fig. 2(a), the characteristic peaks located at 2θ = 41.20° and 43.9° are assigned to (002) and (111) planes of Fe_3N in Fe_3N-FeCo@NC according to the Fe_3N standard PDF (JCPDS 49-1662) [22], and the characteristic peaks observed at 2θ = 44.9° and 65.1° match well with the (110) and (200) planes of FeCo alloy NPs (JCPDS 49-1568) [23]. In comparison, the reference sample Fe/NC derived from the calcination of Fe-PDA in the absence of Co and melamine only exhibits a small peak belonging to the (111) plane of Fe_3N, indicating its low content in Fe/NC. Graphitic carbon exists in both samples as revealed by the broad XRD diffraction peak at around 2θ = 21°. The scanning electron microscopy (SEM) and transmission electron microscopy (TEM) images of Fe_3N-FeCo@NC demonstrate the coexistence of carbon nanospheres and carbon

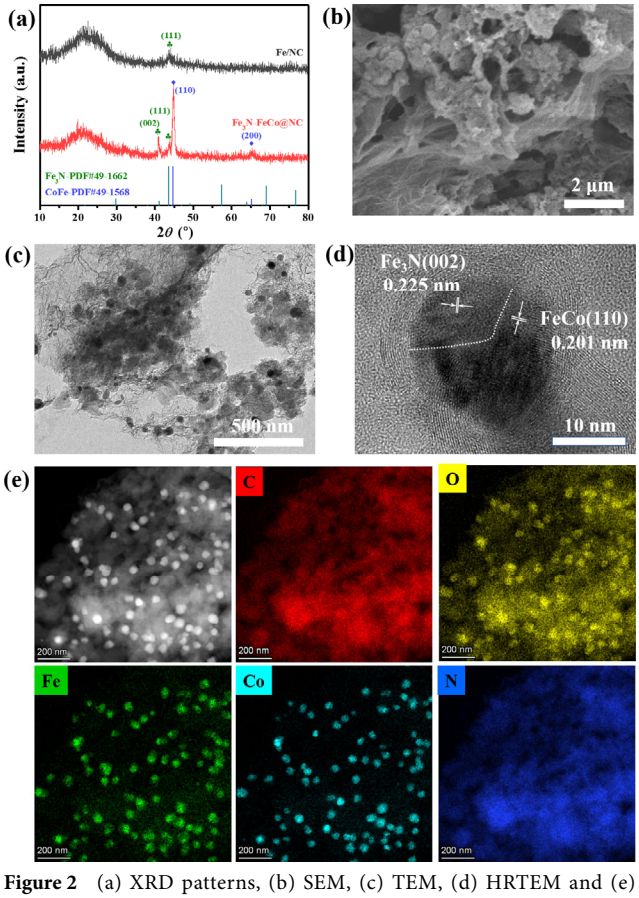

Figure 2 (a) XRD patterns, (b) SEM, (c) TEM, (d) HRTEM and (e) elemental mapping images of Fe_3N-FeCo@NC.

nanosheets, and Fe_3N-FeCo hybrid particles with diameter ranging from 20 to 40 nm are primarily concentrated on spherical carbon (Figs. 2(b) and 2(c)). The high-resolution TEM image shown in Fig. 2(d) indicates that the Fe_3N-FeCo NPs is tightly wrapped by several graphitic carbon layers. The lattice fringe with a *d*-spacing of 0.201 nm is attributed to the (110) plane of FeCo alloy [23], while the lattice distance of 0.225 nm belongs to the (002) plane of Fe_3N [24]. The elemental mapping analysis shows the homogeneous distribution of C, O, Fe, Co and N in Fe_3N-FeCo@NC, and the well-matched Fe and Co signals further signify the FeCo alloy NPs (Fig. 2(e)). It is worth noting that the obvious overlapping of O with Fe and Co is resulted from the surface oxidation of the metal NPs. Comparatively, the control sample Fe/NC only inherits the spherical morphology of Fe-PDA (Fig. S3 in the ESM).

The intrinsic chemical composition of Fe_3N-FeCo@NC was further investigated by X-ray photoelectron spectroscopy (XPS). The survey spectrum (Fig. 3(a)) indicates the presence of C, O, N, Fe, Co, and the corresponding content is 81.5%, 9.0%, 7.9%, 0.9% and 0.7%, respectively. The surface oxidation may account for the O element in Fe_3N-FeCo@NC. The deconvoluted N 1s XPS spectrum as shown in Fig. 3(b) indicates the existence of four N-species, i.e., graphitic-N, pyrrolic-N, metal-N_x and pyridinic-N at the binding energy of 401.40, 400.50, 399.31, and 398.37 eV, respectively [25]. It is noteworthy that the graphitic-N and pyridinic-N can regulate the electronic structure of adjacent carbon atoms and promote O_2 absorption, leading to greatly improved ORR activity [26]. In the high-resolution Fe 2p spectrum, the two peaks located at 707.00 and 720.10 eV are assigned to $2p_{3/2}$ and $2p_{1/2}$ in Fe^0, signifying the metallic Fe in FeCo alloy NPs. The two peaks centered at 709.50 and 722.60 eV belong to $2p_{3/2}$ and $2p_{1/2}$ of Fe^{2+}, consisting with the Fe–N characteristic bond [27]. The two peaks at 712.90 and 726.00 eV are designated to $2p_{3/2}$ and $2p_{1/2}$ of Fe^{3+} [28]. The Co 2p spectrum is depicted in Fig. 3(d), containing Co^0 (780.00/794.99 eV), Co^{2+} (782.69/797.68 eV) and satellite peaks (787.00/802.00 eV) [29]. The high-resolution C 1s spectra (Fig. S4 in the ESM) are deconvoluted into C=C–C, C–N (C=N) and C–O at 284.80, 286.38 and 288.15 eV, respectively [30]. Notably, C=C–C and C–N species are confirmed to be beneficial for ORR [31, 32].

N_2 adsorption–desorption experiments were performed to further reveal the porous structure of Fe_3N-FeCo@NC. The Fe_3N-FeCo@NC exhibits an IV-type isotherm with an obvious hysteresis loop, suggesting a mesoporous structure (Fig. 3(e)). The presence of the macropores is demonstrated by the vertical tails at the relative pressure approach ~ 1.0 for both Fe_3N-FeCo@NC and Fe/NC. The Brunauer–Emmett–Teller (BET) surface area (S_{BET}) of Fe_3N-FeCo@NC is calculated to be 509.82 $m^2 \cdot g^{-1}$, and the total pore volume is 0.819 $cm^3 \cdot g^{-1}$. In comparison, the S_{BET} and total pore volume of Fe/NC are measured to be 368.68 $m^2 \cdot g^{-1}$ and 0.540 $cm^3 \cdot g^{-1}$, respectively. The pore-size distribution depicted in Fig. 3(f) also uncloses the conexistent of meso- and macro-pores in Fe_3N-FeCo@NC. The high S_{BET}, and large pore volume together with the hierarchical porous structure of Fe_3N-FeCo@NC are expected to accelerate ORR kinetics greatly.

3.3 ORR performance

The incorporation of Fe_3N and FeCo alloy NPs into the sphere-/sheet-hybridized carbon with large surface area and hierarchical porous architecture enables the Fe_3N-FeCo@NC as an attractive ORR electrocatalyst. The ORR performance of Fe_3N-FeCo@NC was thus evaluated by linear sweep voltammetry (LSV) recorded on the rotating disk electrode (RDE) in O_2-saturated alkaline electrolyte (i.e., 0.1 M KOH). We first investigated the ORR activity of Fe_3N-FeCo@NC-*x*-*y* with various Fe and Co amounts. As shown in Fig. S5 in the ESM, the optimal Fe and Co contents are found to be 0.010 and 0.15 according to the LSV polarization curves of Fe_3N-FeCo@NC-*x*-*y*. The ORR performance considering of on-set potential (E_{on}), half-wave potential ($E_{1/2}$) and limiting current density (J_L) of the as-prepared samples are summarized in Table S1 in the ESM. The temperature-dependent ORR activity of Fe_3N-FeCo@NC-0.010-0.15 is also scrutinized (Fig. S6 in the ESM), and the sample carbonized at 800 °C delivers the optimum ORR performance owing to the well-balanced conductivity and dispersion of active species [33].

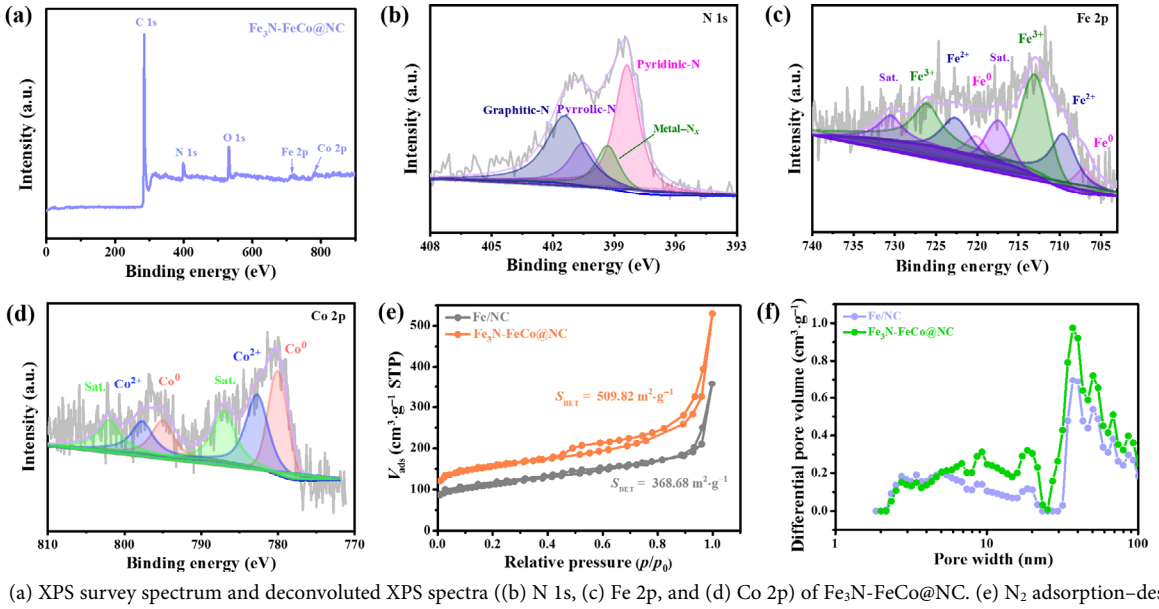

Figure 3 (a) XPS survey spectrum and deconvoluted XPS spectra ((b) N 1s, (c) Fe 2p, and (d) Co 2p) of Fe_3N-FeCo@NC. (e) N_2 adsorption–desorption isotherms and (f) pore size distribution of Fe_3N-FeCo@NC.

The sample Fe_3N-FeCo@NC-0.010-0.15-800 with the highest ORR activity is thus abbreviated as Fe_3N-FeCo@NC in this work.

To systematically examine the ORR performance of Fe_3N-FeCo@NC, three reference samples of Fe/NC (without Co and melamine), Fe,Co/NC (without melamine) and the commercial Pt/C were examined at identical condition. As shown in Fig. 4(a), the Fe_3N-FeCo@NC delivers higher E_{on} and $E_{1/2}$ as compared with Pt/C, Fe/NC and Fe,Co/NC, and the J_L is comparable to that of Pt/C (Table S2 in the ESM). In sharp contrast, Fe/NC demonstrates the lowest E_{on} and $E_{1/2}$. The incorporation of Co can slightly improve the $E_{1/2}$ of the resultant Fe,Co/NC. As we know, the $E_{1/2}$ value is commonly employed to estimate the ORR activity [32]. Thereby, the electrocatalysts measured above have the following order toward ORR based on $E_{1/2}$: Fe_3N-FeCo@NC (0.89 V) > Pt/C (0.85 V) > Fe,Co/NC (0.84V) > Fe/NC (0.81V). The highest ORR activity of Fe_3N-FeCo@NC can be attributed to the synergistic effect of multi-doping, large surface area and hierarchical porous architecture. The simultaneously embedded Fe_3N and FeCo alloy NPs into the carbon matrix is the main reason for the greatly enhanced ORR performance. The large S_{BET} and pore volume significantly improve the accessible active sites in Fe_3N-FeCo@NC. Additionally, the porous sphere and sheet hybridized carbon scaffold may also facilitate the mass transfer pathway. We have also prepared the Fe-NC derived from Fe-PDA without F127 (denoted Fe-NC (no F127)), which exhibits much lower J_L compared with Pt/C (4.44 vs. 5.38 mA·cm^{-2}) (Fig. S7 in the ESM), yet the J_L value Fe/NC is close to Pt/C, illustrating the porous structure is positive for the enhanced ORR performance. At different rotating speeds, the J_L of Fe_3N-FeCo@NC increases with increasing rotating speeds, while the E_{on} is unchanged (Fig. 4(b)). The Koutecky-Levich (K-L) plots display an excellent linear relationship with an average electron transfer number close to 4, manifesting the 4e$^-$ pathway in ORR (Fig. 4(c)). Moreover, the currents of disk (i_d) and ring (i_r) were measured by using the rotating ring disk electrode (RRDE) (Fig. S8(a) in the ESM). The calculated average electron transfer number (3.9) coincides with the K-L plots, and the HO_2^- % is low than 5% (Fig. S8(b) in the ESM), further substantiating the 4e$^-$ pathway. The Tafel slope of Fe_3N-FeCo@NC is determined to be 51.4 mV·dec^{-1}, which is obviously lower compared with Pt/C (64.7 mV·dec^{-1}), manifesting a faster ORR kinetics for Fe_3N-FeCo@NC [34]. Impressively, the ORR performance of Fe_3N-FeCo@NC is competitive with that of previously reported Fe_3N or Fe-N incorporated carbon materials, as summarized in Table S3 in the ESM.

To demonstrate the practical application, the stability and methanol-resistance of Fe_3N-FeCo@NC were recorded. After continuous chronoamperometric measurement (i–t) for 10,000 s in 0.1 M KOH, the Fe_3N-FeCo@NC catalyst possesses 92.5% of its original current. Yet, the current of Pt/C catalyst is significantly decreased to 77%, indicating the superior long-term stability of Fe_3N-FeCo@NC. The addition of methanol causes negligible influence on the current of Fe_3N-FeCo@NC, which contrasts sharply to the dramatically current drop of Pt/C, signifying the outstanding methanol tolerance of Fe_3N-FeCo@NC.

3.4 Zn-air batteries performance

The excellent ORR activity and prominent durability of Fe_3N-FeCo@NC have triggered the exploration as the air-cathode for Zn-air batteries. As depicted in Fig. 5(a), a home-made Zn-air battery using Fe_3N-FeCo@NC as the air-cathode, Zn plate as the anode, and 6 M KOH as the electrolyte is assembled. The open-circuit voltage of Fe_3N-FeCo@NC-equipped Zn-air battery is 1.50 V, higher over that of the Pt/C-based device (Fig. 5(b)). The discharge polarization curves and the power densities of Fe_3N-FeCo@NC-equipped Zn-air battery are shown in Fig. 5(c). Obviously, the Fe_3N-FeCo@NC-equipped Zn-air battery exhibits an obvious higher discharge potential compared to Pt/C. Intriguingly, the maximum power density of Fe_3N-FeCo@NC-based device is up to 141 mW·cm^{-2}, much higher than that of Pt/C counterpart (113 mW·cm^{-2}). Galvanostatic discharge measurements (Fig. 5(d)) indicate

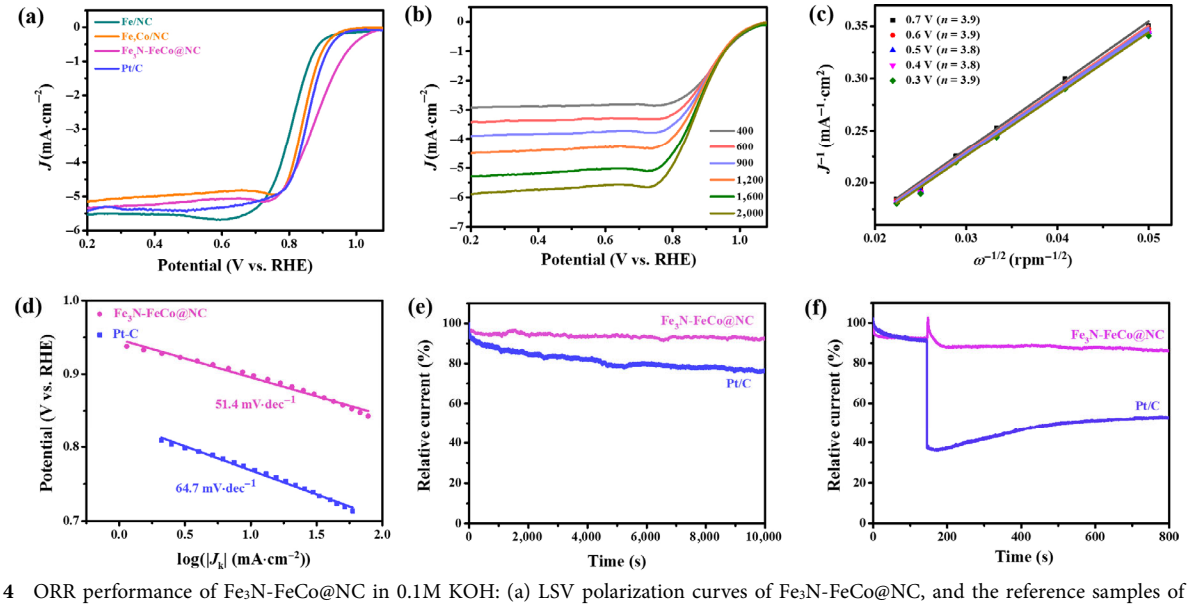

Figure 4 ORR performance of Fe_3N-FeCo@NC in 0.1M KOH: (a) LSV polarization curves of Fe_3N-FeCo@NC, and the reference samples of Fe/NC, Fe,Co/NC and Pt/C at 1,600 rpm; (b) LSV polarization curves of Fe_3N-FeCo@NC at various speeds; (c) K–L plots and the corresponding electron transfer numbers at different potentials; (d) Tafel slopes of Fe_3N-FeCo@NC, and Pt/C; (e) chronoamperometric response (i–t) and (f) methanol resistance of Fe_3N-FeCo@NC.

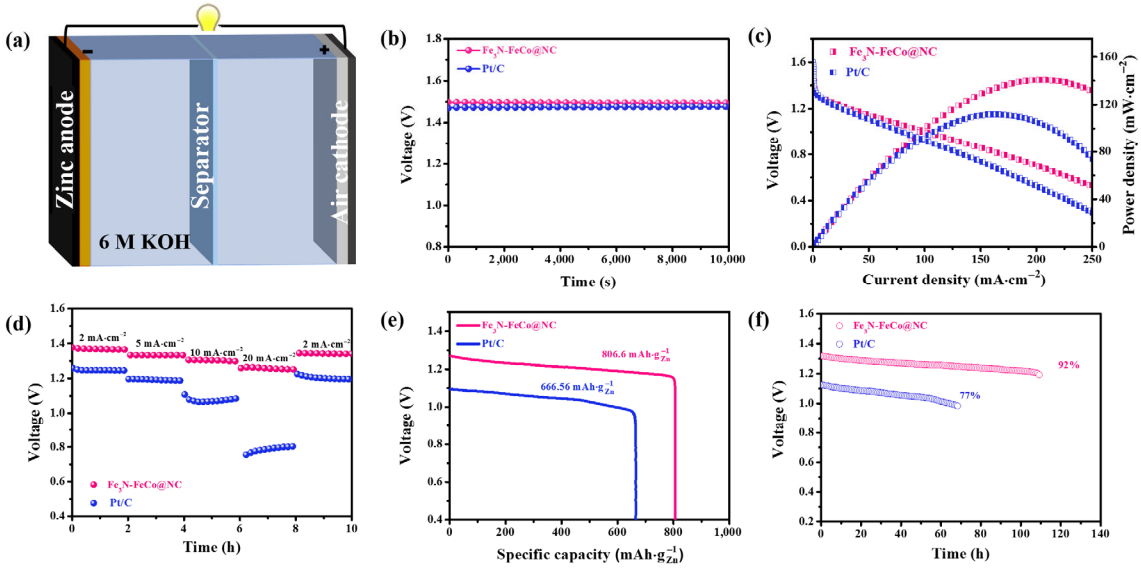

Figure 5 (a) Schematic of the primary Zn-air battery. (b) Open circuit voltages, (c) power density curves, (d) galvanostatic discharge at various current densities, (e) specific capacities, and (f) galvanostatic discharge at 5 mA·cm^{-2} of the Zn-air batteries using Fe_3N-FeCo@NC and Pt/C as air-electrodes, respectively, in 6 M KOH electrolyte.

that the Fe_3N-FeCo@NC-based device displays the potential plain at 1.372, 1.333, 1.301 and 1.251 V at discharge current densities of 2, 5, 10 and 20 mA·cm^{-2}, respectively, and the negligible voltage drop is observed for 2 h. The discharge potential is nearly recovered when a 2 mA·cm^{-2} current is applied again, indicating the excellent rate capability [35]. The Fe_3N-FeCo@NC-based Zn-air battery also exhibits a larger specific capacity (806.6 mAh·g$^{-1}_{Zn}$) at 5 mA·cm^{-2} than Pt/C (660.56 mAh·g$^{-1}_{Zn}$) counterpart (Fig. 5(e)). Notably, there is no obvious potential drop under galvanostatic discharge for 110 h at 5 mA·cm^{-2}, corroborating the superior stability toward ORR catalysis (Fig. 5(f)). Therefore, the performance of Fe_3N-FeCo@NC-equipped Zn-air battery is remarkably increased compared with the Pt/C-based device, and also outperforms most reported Zn-air batteries with Fe_3N or Fe-N containing air-cathode carbon materials as summarized in Table S4 in the ESM. Undoubtedly, the Fe_3N-FeCo@NC can be utilized as a highly efficient and ultra-stable ORR catalyst for the realistic application of Zn-air battery.

4 Conclusions

In conclusion, we report a facile and robust strategy for the preparation of Fe_3N and FeCo alloy NPs embedded carbon nanospheres and nanosheets hybridized composite (denoted Fe_3N-FeCo@NC) by the step-wise pyrolysis of the unique complex composed of metal-coordinated porous PDA nanospheres and melamine. The rational fabrication of metal-coordinated PDA porous nanospheres plays a vital role in the creation of Fe_3N-FeCo@NC, which not only provides the active species (i.e., Fe_3N, FeCo) but also enlarges the specific surface area and facilities the exposure of active sites. The resultant Fe_3N-FeCo@NC catalyst demonstrates impressive ORR performance with a higher E_{on} and a higher $E_{1/2}$ (+40 mV) than Pt/C, and the long-term stability and methanol tolerance of Fe_3N-FeCo@NC also outperform those of the Pt/C catalyst. In addition, the two-electrode Zn-air battery is assembled by using Fe_3N-FeCo@NC as the air-cathode. Impressively, the Fe_3N-FeCo@NC-equipped Zn-air battery exhibits a large power density of 141 mW·cm^{-2}, a high specific capacity of 806.6 mA·h·g$^{-1}_{Zn}$, and a stable galvanostatic discharge time for 110 h at 5 mA·cm^{-2}, which are significantly higher than those of Pt/C-based device. Therefore, the as-synthesized Fe_3N-FeCo@NC catalyst represents a promising and cost-effective alternative to substitute the Pt/C catalyst for the large-scale application of renewable energy technology.

Declaration of conflicting interests

The authors declare no conflicting interests regarding the content of this article.

Acknowledgements

This work was supported by the National Natural Science Foundation of China (No. 52173207), the Natural Science Foundation of Hunan Province (Nos. 2022JJ30563 and 2020JJ5542), and the Outstanding Youth Fund Project of Hunan Provincial Department of Education (No. 21B0119).

Electronic Supplementary Material: Supplementary material (characterization, electrochemical measurements, assemble of Zn-air battery, figures on SEM, FTIR, LSV of as-prepared samples, and tables about BET data and ORR performance) is available in the online version of this article at https://doi.org/10.26599/NRE.2022.9120027.

References

[1] Wang, J.; Kong, H.; Zhang, J. Y.; Hao, Y.; Shao, Z. P.; Ciucci, F. Carbon-based electrocatalysts for sustainable energy applications. *Prog. Mater. Sci.* **2021**, *116*, 100717.

[2] Yan, Y.; Liang, S.; Wang, X.; Zhang, M. Y.; Hao, S. M.; Cui, X.; Li, Z. W.; Lin, Z. Q. Robust wrinkled MoS_2/N-C bifunctional electrocatalysts interfaced with single Fe atoms for wearable zinc-air batteries. *Proc. Natl. Acad. Sci. USA* **2021**, *118*, e2110036118.

[3] Gu, J. W.; Peng, Y.; Zhou, T.; Ma, J.; Pang, H.; Yamauchi, Y. Porphyrin-based framework materials for energy conversion. *Nano Res. Energy* **2022**, *1*, e9120009.

[4] Peng X. W.; Zhang, L.; Chen, Z. X; Zhong, L. X; Zhao, D. K; Chi, X.; Zhao, X. X.; Li, L. G.; Lu, X. H.; Leng, K. et al. Hierarchically porous carbon plates derived from wood as bifunctional ORR/OER electrodes. *Adv. Mater.* **2019**, *31*, 1900341.

[5] Cheng, W. R.; Lu, X. F.; Luan, D. Y.; Lou, X. W. NiMn-based bimetal-organic framework nanosheets supported on multi-channel carbon fibers for efficient oxygen electrocatalysis. *Angew. Chem., Int. Ed.* **2020**, *59*, 18234–18239.

[6] Xiong, Y.; Yang, Y.; DiSalvo, F. J.; Abruña, H. D. Metal-organic-framework-derived Co-Fe bimetallic oxygen reduction electrocatalysts for alkaline fuel cells. *J. Am. Chem. Soc.* **2019**, *141*, 10744–10750.

[7] Liu, L. N.; Yan, F.; Li, K. Y.; Zhu, C. L.; Xie, Y.; Zhang, X. T.; Chen, Y. J. Ultrasmall $FeNi_3N$ particles with an exposed active (110) surface anchored on nitrogen-doped graphene for multifunctional electrocatalysts. *J. Mater. Chem. A* **2019**, *7*, 1083–1091.

[8] Su, C. Y.; Cheng, H.; Li, W.; Liu, Z. Q.; Li, N.; Hou, Z. F.; Bai, F. Q.; Zhang, H. X.; Ma, T. Y. Atomic modulation of FeCo-nitrogen-carbon bifunctional oxygen electrodes for rechargeable and flexible all-solid-state zinc-air battery. *Adv. Energy Mater.* **2017**, *7*, 1602420.

[9] Li, T. F.; Li, M.; Zhang, M. R.; Li, X.; Liu, K. H.; Zhang, M. Y.; Liu, X. E.; Sun, D. M.; Xu, L.; Zhang, Y. W. et al. Immobilization of Fe_3N nanoparticles within N-doped carbon nanosheet frameworks as a high-efficiency electrocatalyst for oxygen reduction reaction in Zn-air batteries. *Carbon* **2019**, *153*, 364–371.

[10] Hao, R.; Chen, J. J.; Wang, Z. Y.; Zhang, J. J.; Gan, Q. M.; Wang, Y. F.; Li, Y. Z.; Luo, W.; Wang, Z. Q.; Yuan, H. M. et al. Iron polyphthalocyanine-derived ternary-balanced Fe_3O_4/Fe_3N/Fe-N-C@PC as a high-performance electrocatalyst for the oxygen reduction reaction. *Sci. China Mater.* **2021**, *64*, 2987–2996.

[11] Qian, Y. D.; Du, P.; Wu, P.; Cai, C. X.; Gervasio, D. F. Chemical nature of catalytic active sites for the oxygen reduction reaction on nitrogen-doped carbon-supported non-noble metal catalysts. *J. Phys. Chem. C* **2016**, *120*, 9884–9896.

[12] Lv, Y. R.; Zhai, X. J.; Wang, S.; Xu, H.; Wang, R.; Zang, S. Q. 3D-ordered macroporous N-doped carbon encapsulating Fe-N alloy derived from a single-source metal-organic framework for superior oxygen reduction reaction. *Chin. J. Catal.* **2021**, *42*, 490–500.

[13] Li, G. X.; Yu, J. Y.; Yu, W. Q.; Yang, L. J.; Zhang, X. L.; Liu, X. Y.; Liu, H.; Zhou, W. J. Phosphorus-doped iron nitride nanoparticles encapsulated by nitrogen-doped carbon nanosheets on iron foam *in situ* derived from *Saccharomycetes cerevisiae* for electrocatalytic overall water splitting. *Small* **2020**, *16*, 2001980.

[14] He, J. K.; Huang, J. Y.; Wang, Z. W.; Liu, Z.; Chen, Y.; Su, R. D.; Ni, X. Y.; Li, Y. W.; Xu, X.; Zhou, W. Z. et al. The enhanced catalytic degradation of sulfamethoxazole over Fe@nitrogen-doped carbon-supported nanocomposite: Insight into the mechanism. *Chem. Eng. J.* **2022**, *439*, 135784.

[15] Radwan, A.; Jin, H. H.; Liu, B. S.; Chen, Z. B.; Wu, Q.; Zhao, X.; He, D. P.; Mu, S. C. 3D-ZIF scaffold derived carbon encapsulated iron nitride as a synergistic catalyst for ORR and zinc-air battery cathodes. *Carbon* **2021**, *171*, 368–375.

[16] Hao, Y. R.; Xue, H.; Lv, L.; Sun, J.; Guo, N. K.; Song, T. S.; Dong, H. L.; Zhang, J. W.; Wang, Q. Unraveling the synergistic effect of defects and interfacial electronic structure modulation of pealike CoFe@Fe_3N to achieve superior oxygen reduction performance. *Appl. Catal. B: Environ.* **2021**, *295*, 120314.

[17] Peng, L.; Hung, C. T.; Wang, S. W.; Zhang, X. M.; Zhu, X. H.; Zhao, Z. W.; Wang, C. Y.; Tang, Y.; Li, W.; Zhao, D. Y. Versatile nanoemulsion assembly approach to synthesize functional mesoporous carbon nanospheres with tunable pore sizes and architectures. *J. Am. Chem. Soc.* **2019**, *141*, 7073–7080.

[18] Chen, F.; Xing, Y. X.; Wang, Z. Q.; Zheng, X. Y.; Zhang, J. X.; Cai, K. Y. Nanoscale polydopamine (PDA) meets π-π interactions: An interface-directed coassembly approach for mesoporous nanoparticles. *Langmuir* **2016**, *32*, 12119–12128.

[19] Zhang, L.; Wang, Q.; Jian, R. K.; Wang, D. Y. Bioinspired iron-loaded polydopamine nanospheres as green flame retardants for epoxy resin via free radical scavenging and catalytic charring. *J. Mater. Chem. A* **2020**, *8*, 2529–2538.

[20] Ding, Y. C.; Xu, W. H.; Yu, Y.; Hou, H. Q.; Zhu, Z. T. One-step preparation of highly hydrophobic and oleophilic melamine sponges via metal-ion-induced wettability transition. *ACS Appl. Mater. Interfaces* **2018**, *10*, 6652–6660.

[21] Wang, T.; He, Y.; Liu, Y. J.; Guo, F. J.; Li, X. F.; Chen, H. B.; Li, H. M.; Lin, Z. Q. A ZIF-triggered rapid polymerization of dopamine renders Co/N-codoped cage-in-cage porous carbon for highly efficient oxygen reduction and evolution. *Nano Energy* **2021**, *79*, 105487.

[22] Xue, N.; Liu, J.; Wang, P. Y.; Wang, C. Y.; Li, S.; Zhu, H.; Yin, J. Scalable synthesis of Fe_3N nanoparticles within N-doped carbon frameworks as efficient electrocatalysts for oxygen reduction reaction. *J. Colloid Interface Sci.* **2020**, *580*, 460–469.

[23] Cui, Z. H.; Liang, X. Z.; Wang, P.; Zhou, P.; Zhang, Q. Q.; Wang, Z. Y.; Zheng, Z. K.; Liu, Y. Y.; Dai, Y.; Huang, B. B. *In situ* integration of Fe_3N@Co_4N@CoFe alloy nanoparticles as efficient and stable electrocatalyst for overall water splitting. *Electrochim. Acta* **2021**, *395*, 139218.

[24] Zhang, Y. P.; Wang, N.; Jia, N.; Wang, J.; Sun, J.; Shi, F.; Liu, Z. H.; Jiang, R. B. A low-cost and facile method for the preparation of Fe-N/C-Based hybrids with superior catalytic performance toward oxygen reduction reaction. *Adv. Mater. Interfaces* **2019**, *6*, 1900273.

[25] Wang, T.; Yang, C.; Liu, Y. J.; Yang, M.; Li, X. F.; He, Y.; Li, H. M.; Chen, H. B.; Lin, Z. Q. Dual-shelled multidoped hollow carbon nanocages with hierarchical porosity for high-performance oxygen reduction reaction in both alkaline and acidic media. *Nano Lett.* **2020**, *20*, 5639–5645.

[26] Li, G. J.; Tang, Y. B.; Fu, T. T.; Xiang, Y.; Xiong, Z. P.; Si, Y. J.; Guo, C. Z.; Jiang, Z. Q. S, N co-doped carbon nanotubes coupled with CoFe nanoparticles as an efficient bifunctional ORR/OER electrocatalyst for rechargeable Zn-air batteries. *Chem. Eng. J.* **2022**, *429*, 132174.

[27] Huang, X. X.; Yang, Z. Y.; Dong, B.; Wang, Y. Z.; Tang, T. Y.; Hou, Y. L. *In situ* Fe_2N@N-doped porous carbon hybrids as superior catalysts for oxygen reduction reaction. *Nanoscale* **2017**, *9*, 8102–8106.

[28] Choi, C. H.; Choi, W. S.; Kasian, O.; Mechler, A. K.; Sougrati, M. T.; Brüller, S.; Strickland, K.; Jia, Q. Y.; Mukerjee, S.; Mayrhofer, K. J. J. et al. Unraveling the nature of sites active toward hydrogen peroxide reduction in Fe-N-C catalysts. *Angew. Chem., Int. Ed.* **2017**, *56*, 8809–8812.

[29] Liu, C.; Wang, J.; Wan, J. J.; Cheng, Y.; Huang, R.; Zhang, C. Q.; Hu, W. L.; Wei, G. F.; Yu, C. Z. Amorphous metal-organic framework-dominated nanocomposites with both compositional and structural heterogeneity for oxygen evolution. *Angew. Chem., Int. Ed.* **2020**, *59*, 3630–3637.

[30] Yu, H.; Zhang, D. D.; Fang, Z.; Xu, S.; Liu, Q.; Hou, H. L.; Wang, L.; Zhou, Z. Y.; Shao, G.; Yang, W. Y. et al. N and S co-doped carbon nanofibers with embedded candle soot and designed surface decoration for efficient bifunctional electrocatalysts. *Electrochim. Acta* **2021**, *380*, 138261.

[31] Wang, C. Y.; Chen, W. X.; Xia, K. L.; Xie, N. H.; Wang, H. M.; Zhang, Y. Y. Silk-derived 2D porous carbon nanosheets with atomically-dispersed Fe-N_x-C sites for highly efficient oxygen reaction catalysts. *Small* **2019**, *15*, 1804966.

[32] Li, X. F.; Liu, Y. J.; Chen, H. B.; Yang, M.; Yang, D. G.; Li, H. M.; Lin, Z. Q. Rechargeable Zn-air batteries with outstanding cycling stability enabled by ultrafine FeNi nanoparticles-encapsulated N-doped carbon nanosheets as a bifunctional electrocatalyst. *Nano Lett.* **2021**, *21*, 3098–3105.

[33] Jannath, K. A.; Huang, Y. H.; Seo, K. D.; Park, D. S.; Shim, Y. B. Fe_3N decorated S/N doped carbon derived from a coordinated polymer as a bifunctional electrocatalyst for oxygen reduction and catecholamines oxidation. *Carbon* **2022**, *187*, 1–12.

[34] Yan, P.; Kong, D. W.; Yuan, W. J.; Xie, A. J.; Shen, Y. H. *In situ* synthesis and electrocatalytic performance of Fe/$Fe_{2.5}C$/Fe_3N/nitrogen-doped carbon nanotubes for the oxygen reduction reaction. *ChemElectroChem* **2019**, *6*, 3030–3038.

[35] Qi, D. F.; Lv, F.; Wei, T. R.; Jin, M. M.; Meng, G.; Zhang, S. S.; Liu, Q.; Liu, W. X.; Ma, D.; Hamdy, M. S. et al. High-efficiency electrocatalytic NO reduction to NH_3 by nanoporous VN. *Nano Res. Energy* **2022**, *1*, e9120022.

Fanjuan Guo is now a master student in College of Chemistry at Xiangtan University, China. She is working on the design and synthesis of multi-doped porous carbon materials for energy conversion and storage devices.

Hongbiao Chen is a professor in College of Chemistry at Xiangtan University, China. She received her MS degree in Organic Chemistry at Xiangtan University in 2001 and PhD degree in Polymer Chemistry & Physics at Xiangtan University in 2008. Her research concerns organic synthesis, and porous carbon materials.

Yijiang Liu received her MS degree in Polymer Chemistry & Physics at Xiangtan University in 2009 and PhD degree in Polymer Chemistry & Physics from the Institute of Chemistry, Chinese Academy of Sciences in 2015. Now, she is an associate professor in College of Chemistry at Xiangtan University, China. Her research work focuses on the design and preparation of advanced functional materials, such as high-stable perovskite nanocrystals by using functional polymer as nanoreactors, Janus nanosheets for concurrent catalysis and emulsification, and metal-organic frameworks derived porous carbon materials for efficient and durable electrocatalysts in energy conversion and storage devices. She has published over 34 first/co-first authored papers, including Chemical Society Reviews, Progress in Materials Science, ACS Nano, Nano Letters, Nano Energy, and Macromolecules.